Directional Wavelet Analysis of Inhomogeneity in the Surface Wave Field from Aerial Laser Scanning Data

RICHARD M. GORMAN

National Institute of Water and Atmospheric Research, Hamilton, New Zealand

D. MURRAY HICKS

National Institute of Water and Atmospheric Research, Christchurch, New Zealand

(Manuscript received 14 May 2004, in final form 3 September 2004)

ABSTRACT

Modern measurement techniques such as aerial laser scanning allow for rapid determination of the spatial variation of sea surface elevation. Wave fields obtained from such data show spatial inhomogeneity associated with the presence of wave groups. A method based on two-dimensional directional wavelet analysis is described by which such inhomogeneity can be characterized in the spatial and wavenumber domains. The directional wavelet method has been applied to aerial laser scanning measurements of nearshore wave conditions off the east coast of New Zealand's South Island. A high level of spatial variability was observed, with evidence of ensembles of wave-group envelopes of quasi-Gaussian form. These envelopes occur, with variations in spatial location, across a range of wavelet scales and directions.

1. Introduction

A signal recorded as a time series carries information that can be studied either by considering its time evolution or by analyzing its frequency content. In the time domain, one obtains information at the minimum temporal resolution Δt, but loses all spectral information, while a Fourier spectral representation gives fine resolution Δf in the frequency domain, but cannot provide any information that specifies the times at which various frequencies are prominent. A surface wave record from the ocean is a good example, as periodic motions with well-defined frequencies are often prominent in the record, but the strength of these periodic signals is normally quite variable over longer time frames. So analysis in the frequency domain is valuable, but any implication that the mix of frequencies given by the Fourier spectrum applies equally throughout the recording period may be quite misleading (Liu 2000a,b).

A more appropriate representation should combine these complementary descriptions in the time and frequency domains. Indeed, there is no perfect representation due to the lower limit on the product $\Delta t \Delta f$ resulting from the uncertainty principle, which prevents us from simultaneously localizing information from the signal perfectly in both time and frequency. But a compromise, accepting moderate resolution in both time and frequency, can be sought. In one approach, Gabor (1946) proposed the windowed Fourier transform, which introduces some time locality by convolving the signal with a set of Fourier modes localized in a Gaussian envelope of constant width a_0. This transform allows a time-frequency decomposition of the signal at a given scale a_0, which is kept fixed.

More recently, Grossmann and Morlet (1984) devised a wavelet transform, which is implemented by convolving the signal with a set of analyzing wavelets $\psi_{a,b}$ obtained by dilation and translation of a given function $\psi(t)$ representing at least one oscillation. The wavelet transform realizes the best compromise in view of the uncertainty principle, because it adapts the time-frequency resolution $\Delta t \Delta f$ to each scale a. In fact it gives a fine spectral resolution Δf with a coarse time resolution Δt in the large scales, while on the other hand giving a fine time localization Δt with a coarse spectral resolution Δf in the small scales.

The wavelet transform has become a widely used tool in signal processing (e.g., Chui et al. 1994; Daubechies 1990, 1992), starting with its early application to seismic data (Goupillaud et al. 1984). Applications to ocean surface wave data are now becoming more common to investigate the nonstationary properties of wave records in the time domain (Liu 2000a,b). Also, Donelan et al. (1996) have derived wavelet methods for

Corresponding author address: Dr. Richard Gorman, NIWA, P.O. Box 11115, Hamilton, New Zealand.
E-mail: r.gorman@niwa.co.nz

computing directional spectra from sets of time series data, making use of a representation of the sea state as a superposition of wave groups (Mollo-Christensen and Ramamonjiarisoa 1978).

A similar view can be taken of the sea state in the spatial domain. A snapshot of the sea surface will show wave crests and troughs with a certain periodicity, and a two-dimensional Fourier analysis will provide a directional wavenumber spectrum identifying the contribution of wave components with various wavelengths and propagation directions, but will not indicate the spatial variability of the wave field associated with the presence of wave groups.

The continuous wavelet transform has been extended to two and higher dimensions by Murenzi (1989). In two dimensions, the wavelet transform provides directional information as well as scaling and translation in both coordinates. The resulting directional wavelet transform found an initial application in studying diffusion-limited aggregates and other two-dimensional fractals (Argoul et al. 1989) and has since been applied to turbulence studies (Farge 1990; Farge et al. 1993). The directional wavelet transform is also used in image analysis, with particular value in edge detection (Antoine and Murenzi 1996; Antoine et al. 1996).

Spedding et al. (1993) applied 2D wavelet methods to surface wave data, recorded as video imagery of flume experiments that observed wave growth under wind forcing. Using both nondirectional and direction-specific (Morlet) wavelets, they were able to observe differences between spatial distributions of energy at harmonic and subharmonic scales. They also detected growth in wave energy at directions away from the mean wind direction. Their results were limited, however, by the indirect and uncertain relationship between image intensity data and the water surface elevation for which it was a surrogate. It could also be said that the formulation is made slightly less elegant by not incorporating directional properties explicitly into the wavelet transform, as is done in the fully directional formulation (Antoine and Murenzi 1996; Antoine et al. 1996). Little has since been done to follow up the initial work of Spedding et al. (1993) in laboratory applications, or in field studies.

The advent of remote sensing techniques such as aerial laser scanning allows for rapid determination of the spatial variation of sea surface elevation, at a scale that provides information at subwavelength scales over spatial domains large enough to reveal inhomogeneity associated with the presence of wave groups. It seems timely, then, to consider the use of two-dimensional directional wavelet analysis to characterize such inhomogeneity in both spatial and wavenumber domains.

In July 2001, a set of aerial laser scanning measurements was made over the east coast of New Zealand's South Island. The coverage area included scanning of coastal waters, providing records of nearshore wave conditions. In this paper we describe the use of directional wavelet methods, as applied to this dataset.

2. The directional continuous wavelet transform

In oceanographic studies, wavelet methods have to date mostly been applied to studies in the time domain. In that case, we might wish to investigate a time series $s(t)$ of data collected at uniform intervals of time t. This can be done by defining a convolution

$$S(a, b) = a^{-1/2} \int dt\, \overline{\psi}[a^{-1}(t - b)]s(t) \tag{1}$$

of the data with a defined analyzing wavelet function ψ applied on a time domain that has been translated by an offset b and stretched by a scale parameter a. The overbar denotes complex conjugation. Equation (1) defines the continuous wavelet transformation, which can be considered as representing the amount of variation in the data of periodicity corresponding to the scale a, localized at the time b.

It is necessary to choose an analyzing or "mother" wavelet function appropriate for a particular application. One of the practical guiding principles is to choose a mother wavelet that has a similar shape and characteristics to the signals expected in the data. In wave studies in the time domain, the Morlet wavelet, consisting of a complex sinusoidal function under a Gaussian envelope, has proven a suitable choice, being well localized in both time and frequency (Donelan et al. 1996).

It is possible to extend this method to two dimensions. We might, for example, consider a scalar quantity $s(\mathbf{x})$ measured over a horizontal plane as a function of spatial coordinates $\mathbf{x} = (x, y)$. While the unitary linear transformations that can be applied to a one-dimensional variable are restricted to scaling and translation, in two dimensions we can have scaling, translations in both dimensions, and rotation. Hence the two-dimensional continuous wavelet transform can be defined as

$$S(a, \theta, \mathbf{b}) = c_\psi^{-1/2} a^{-1} \int d^2\mathbf{x}\, \overline{\psi}[a^{-1} r_{-\theta}(\mathbf{x} - \mathbf{b})]s(\mathbf{x}). \tag{2}$$

The linear transformations applied to the analyzing wavelet extend to include scaling by a factor a, translation by a vector $\mathbf{b}$, and rotation by an angle θ, via the rotation operator

$$r_\theta = \begin{pmatrix} \cos\theta & -\sin\theta \\ \sin\theta & \cos\theta \end{pmatrix}. \tag{3}$$

The continuous wavelet transformation can be more conveniently calculated using Fourier transforms:

$$S(a, \theta, \mathbf{b}) = a \int d^2\mathbf{k}\, e^{i\mathbf{b}\cdot\mathbf{k}}\, \overline{\hat{\psi}}[a r_{-\theta}(\mathbf{k})]\hat{s}(\mathbf{k}), \tag{4}$$

where $\hat{s}(\mathbf{k})$ is the Fourier transform of $s(\mathbf{x})$, expressed in terms of wavenumber vectors $\mathbf{k} = (k_x, k_y)$.

The wavelet function must be selected subject to the condition that the normalization constant

$$c_\psi = (2\pi)^2 \int \frac{d^2\mathbf{k}}{|\mathbf{k}|^2} |\hat{\psi}(\mathbf{k})|^2 \tag{5}$$

is finite. For sufficiently regular functions [$\psi \in L^1(R^2, d^2\mathbf{x}) \cap L^2(R^2, d^2\mathbf{x})$], this admissibility condition corresponds to the requirement that

$$\int d^2\mathbf{x}\, \psi(\mathbf{x}) = 0. \tag{6}$$

With these definitions, we can note some properties of the two-dimensional continuous wavelet transform (Antoine and Murenzi 1996; Antoine et al. 1996). First, the transform is linear in the signal $s(\mathbf{x})$, so that linear superpositions of signals in the data will be reflected in corresponding linear superpositions in the wavelet transform $S(a, \theta, \mathbf{b})$. Second, the transform has a conservation of energy property:

$$c_\psi^{-1} \int\int\int \frac{da}{a^3}\, d\theta\, d^2\mathbf{b}\, |S(a, \theta, \mathbf{b})|^2 = \int d^2\mathbf{k} |\hat{s}(\mathbf{k})|^2 = \int d^2\mathbf{x} |s(\mathbf{x})|^2. \tag{7}$$

Third, the transform can be inverted:

$$s(\mathbf{x}) = c_\psi^{-1} \int\int\int \frac{da}{a^3}\, d\theta\, d^2\mathbf{b}\, \psi_{a,\theta,\mathbf{b}}(\mathbf{x}) S(a, \theta, \mathbf{b}). \tag{8}$$

As in the one-dimensional case, it is helpful to choose a mother wavelet of a form representing a localized propagating wave signal. A two-dimensional version of the Morlet wavelet can be defined (Antoine and Murenzi 1996; Antoine et al. 1996), using a subscript M for "Morlet," as

$$\psi_M(\mathbf{x}) = (e^{ik_0 y} - e^{-k_0^2/2}) \exp\left[-\frac{1}{2}(x^2/\varepsilon + y^2)\right]. \tag{9}$$

This is a nonisotropic function, selecting a preferred direction (aligned along the y axis), as well as a base wavenumber k_0. This property makes it suitable for applications where directionality needs to be resolved (e.g., detecting edges and segments in images). The $e^{-k_0^2/2}$ term ensures that the wavelet meets the admissibility criterion (6), but the term is negligible with typical values $k_0 > 5$, and is often omitted. Note that in the general case the asymmetry parameter $\varepsilon \neq 1$, and so the envelope function can be weighted differently in directions parallel and transverse to the preferred direction.

The Fourier transform of the Morlet wavelet is (Antoine and Murenzi 1996; Antoine et al. 1996):

$$\hat{\psi}_M(\mathbf{k}) = \sqrt{\varepsilon} \exp\left\{-\frac{1}{2}[\varepsilon k_x^2 + (k_y - k_0)^2]\right\}, \tag{10}$$

with the $e^{-k_0^2/2}$ term omitted. Retaining it, the Fourier transform becomes

$$\hat{\psi}_M(\mathbf{k}) = \sqrt{\varepsilon}\left\langle \exp\left\{-\frac{1}{2}[\varepsilon k_x^2 + (k_y - k_0)^2]\right\} - \exp\left[-\frac{1}{2}(\varepsilon k_x^2 + k_y^2 + k_0^2)\right]\right\rangle. \tag{11}$$

The normalization factor c_ψ for the Morlet wavelet can be computed numerically, or approximated by a Taylor series (as described in the appendix), from the integral expression (5).

The scale a can be related to wavenumber k by calibrating with a monochromatic sinusoidal wave field and finding the value of a where $|S|$ is a maximum. By analogy with time-domain analysis (Torrence and Compo 1998), for the Morlet wavelet we find an equivalent wavelength

$$\lambda = \frac{4\pi a}{k_0 + \sqrt{2 + k_0^2}}. \tag{12}$$

It should be noted that all values above are dimensionless—that is, we assume a data interval $\delta x = 1$. Dimensionally appropriate values can be obtained by scaling by δx. Hence the equivalent wavenumber corresponding to scale a is

$$k_{\mathrm{eq}} = \frac{k_0 + \sqrt{2 + k_0^2}}{2a\delta x}. \tag{13}$$

3. Application to sea surface data

When we come to apply the continuous wavelet transform to sea surface data, it will be instructive to draw some analogies with standard Fourier spectral methods. Using the correspondence between a and k_{eq}, we can define a wavelet spectrum

$$F(k_{\mathrm{eq}}, \theta, \mathbf{b}) = |S(a, \theta, \mathbf{b})|^2. \tag{14}$$

This quantity is analogous to a directional wavenumber spectrum localized at position $\mathbf{b}$. We can take various moments, including a direction-averaged spectrum

$$F_1(k_{\mathrm{eq}}, \mathbf{b}) = \int d\theta\, F(k_{\mathrm{eq}}, \theta, \mathbf{b}) \tag{15}$$

and a local variance, or energy density:

$$E_0(\mathbf{b}) = \int\int k_{\mathrm{eq}}\, dk_{\mathrm{eq}}\, d\theta\, F(k_{\mathrm{eq}}, \theta, \mathbf{b}) \propto \int\int \frac{da}{a^3}\, d\theta\, |S(a, \theta, \mathbf{b})|^2. \tag{16}$$

The quantity $4(E_0)^{(1/2)}$ is analogous to a localized significant wave height. From the "conservation of energy" relationship (7), we note that the spatial average of E_0 is proportional to the total variance in the data.

4. Waitaki River aerial laser scanning data

Surface elevation data were obtained from an aerial laser scanning (ALS) survey of the vicinity of the lower Waitaki River, a braided river flowing to the east coast of the South Island of New Zealand (Fig. 1). Scanning was conducted in July 2001 by AAM Geoscan of Australia using an Optech ALTM1225 ALS system (Hicks et al. 2001, 2003).

Data were collected in swaths of approximately 800-m width, with the laser scanning back and forth in sweeps transverse to the aircraft's flight path. The sweep frequency was 28 Hz, laser pulse frequency was 16000 Hz, flying height was approximately 1100 m, and the flight speed was approximately 56 m s^{-1} (200 km h^{-1}). As a result, the surface elevation was sampled in a zigzag path, with sample points spaced at approximately 1-m intervals along each sweep and successive sweeps crossing under the flight path at intervals of less than 1 m. This resulted in an average sample point spacing of 1.2 m. The vertical accuracy of ground elevation measurements was checked against 207 ground-surveyed test points. This showed a standard error of 5 cm for points that collocated with a laser "shot" and 8 cm for points interpolated from nearby laser shots. The ALS data were located within the New Zealand map grid (NZMG) coordinate system (Fig. 1b) and referenced to the Lyttelton mean sea level datum. The latter involved establishing a local geoid model across the project area from 25 control points for which both WGS84 ellipsoidal and Lyttelton datum orthometric heights were known (Williams and Jonas 2001).

The dataset includes several swaths over water (Fig. 1b). Of these, we selected one transect that was flown running shore-normal, crossing the coast near the Waitaki River mouth. Data were collected along this transect on successive days: "swath 2.6" was recorded on 11 July 2001 (Fig. 2), and "swath 2.9" was recorded on 12 July 2001 (Fig. 3). In these figures, data are shown in local coordinates (x, y) rotated by –76.7° from north about an origin at NZMG coordinates (5583463N, 2365026E) to align with the flight direction, and interpolated onto a rectangular grid at 5-m resolution.

At normal river flows, the Waitaki River mouth consists of an elongated lagoon behind a wave-built gravel barrier. The lagoon drains to the ocean via a relatively narrow channel that is often offset northward of the river channel center line. During floods, the river cuts a wide breach in the barrier and deposits a submerged delta offshore. This delta material is subsequently transported shoreward by waves, accretes to the barrier, and is eventually transported northward by longshore drift. Waves approaching the coast at the river mouth are locally refracted by any remnant submerged delta. Shore-normal bathymetry profiles sounded in 1977 (Fig. 4) indicate that the remnant delta topogra-

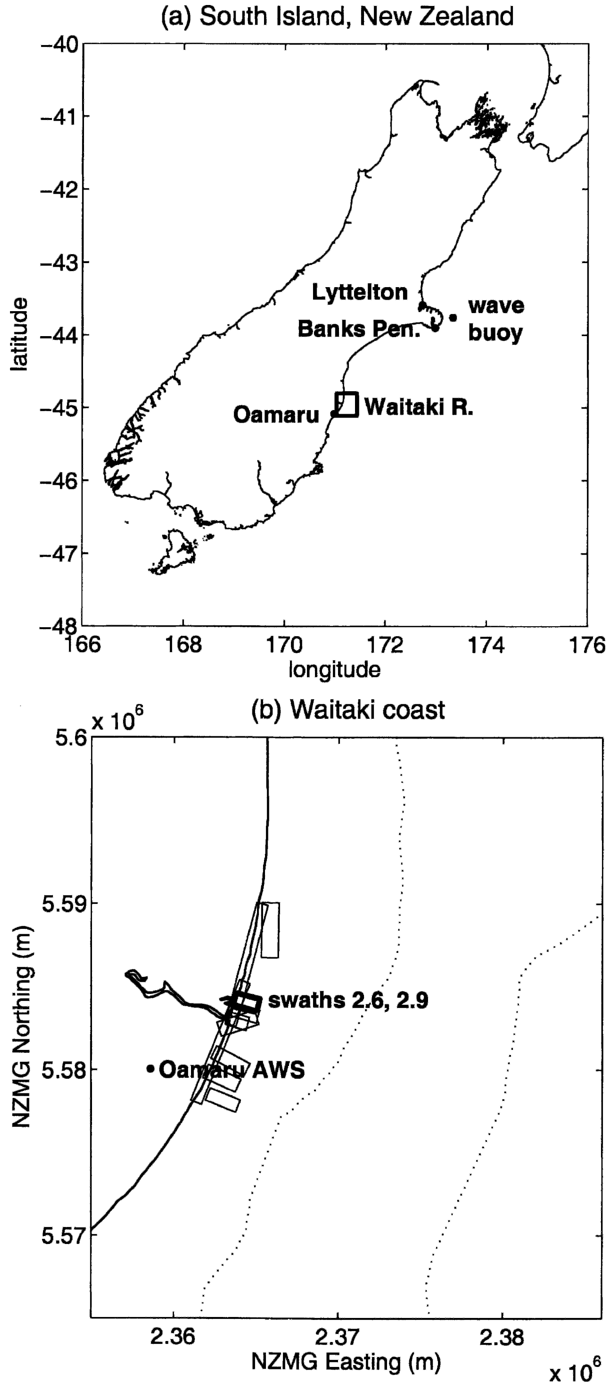

FIG. 1. Location maps of (a) the South Island of New Zealand, showing the location of the Waitaki River study region and the Banks Peninsula wave buoy, and (b) the coast adjacent to the Waitaki River mouth. Boxes show where ALS swaths were taken that include sea coverage. Those referred to in the text are marked by boldface lines. The dotted lines mark the 20- and 50-m isobaths.

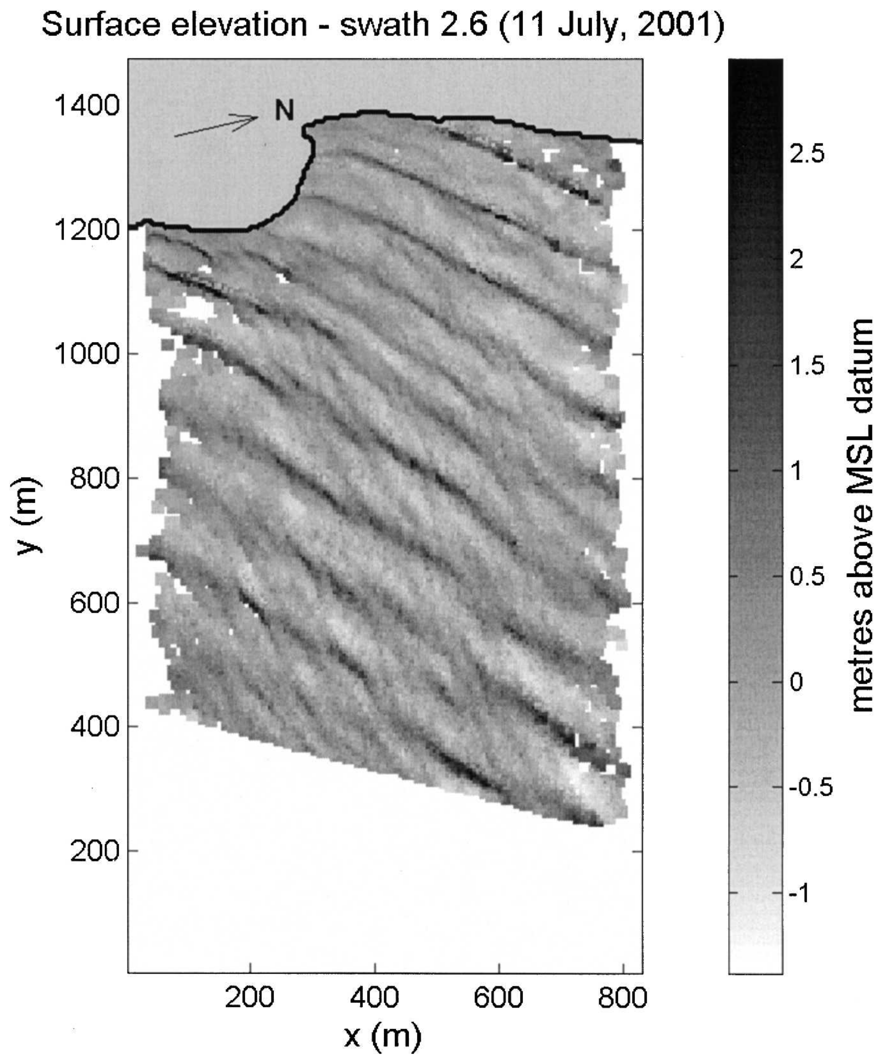

FIG. 2. Surface elevation $s(\mathbf{x})$ gridded at 5-m spacing from a shore-normal ALS swath (swath 2.6) crossing the coast near the Waitaki River mouth. Data were recorded on 11 Jul 2001. Data are shown in local coordinates (x, y) rotated to align with the flight direction. The shoreline is marked by a solid line, and north is marked by an arrow.

phy may rise at least 2 m above the normal nearshore profile, (as represented by a profile surveyed south of the river mouth). The regions covered by the ALS swaths in 2001 were all in shallow water of less than 10-m depth. However no detailed bathymetry data were available at comparable resolution to the ALS data.

Wave conditions off the South Island east coast during this period are available from a wave buoy located in 76-m water depth off Banks Peninsula, some 200 km to the northeast (Fig. 1a). Significant wave heights at the buoy site rose from 2–3 m during the 11 July survey to approximately 4 m on 12 July (Fig. 5). Both mean and peak wave periods were also higher on 12 July (T_{peak} = 13–14 s) than on 11 July (T_{peak} = 11–12 s), while mean wave direction remained close to 180° (from the south) throughout. From linear wave theory we expect waves of 11- and 14-s periods to have wavelengths of 103 and 134 m, respectively, in 10-m water depth.

The ALS data show an apparent increase in wavelengths from 11 to 12 July. The principal wave direction evident in the ALS data is from the southeast, differing from the southerly mean wave direction off Banks Peninsula, most likely because of a difference in exposure combined with refraction. There also appears to be a shorter wavelength pattern present on both days consistent with wind sea from a more southerly direction.

Wind data were available from the nearby Oamaru Automated Weather Station (Fig. 1b). During the 11 July survey, winds were from the westerly quadrant (i.e., offshore), with speeds less than 4 m s^{-1} (Fig. 5). The following day the wind shifted through southwest

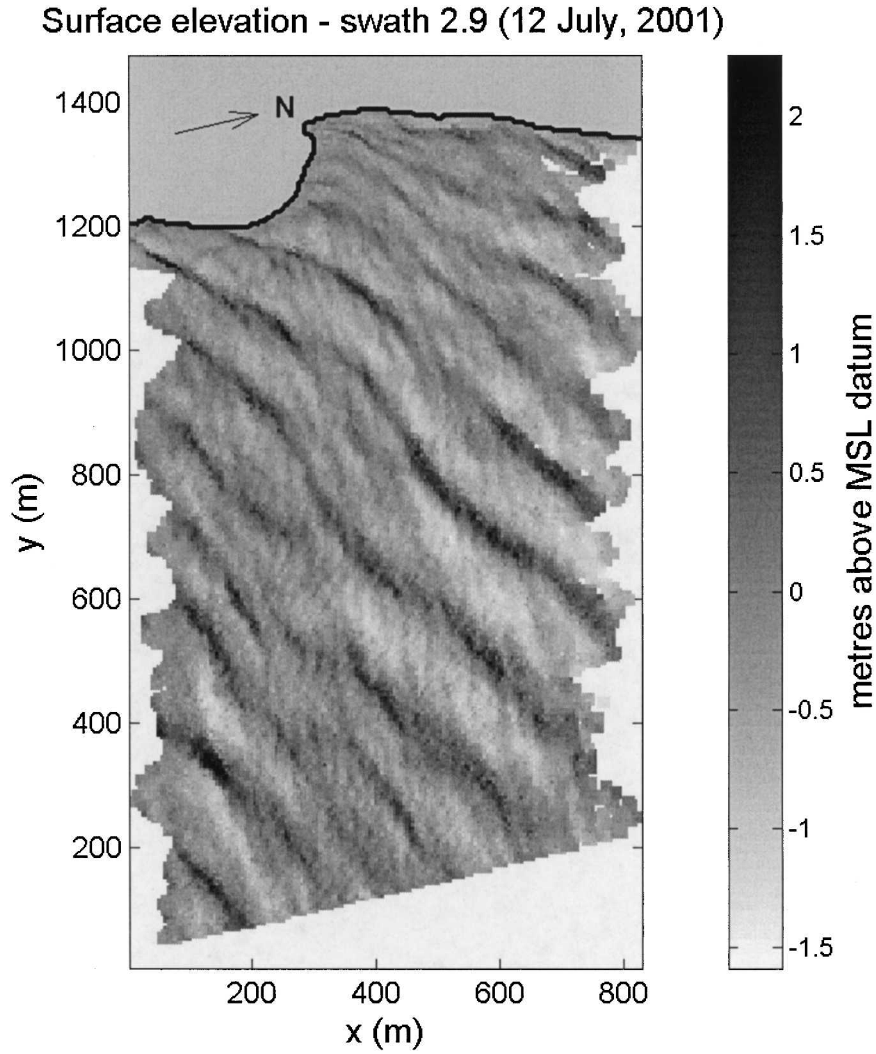

FIG. 3. As in Fig. 2 except data were recorded on 12 Jul 2001.

to southerly, with variable speeds in the 3–7 m s^{-1} range.

Swath 2.6 was recorded flying in the seaward direction, while swath 2.9 was flown shoreward. Because a transect is flown in a finite time, the ALS record is not truly instantaneous. Rather, the movement of the waves during the scan produces a Doppler effect. Waves moving with a positive velocity component in the aircraft's flight direction appear elongated in wavelength by the distance a crest moves while the aircraft moves between overtaking successive crests. Conversely, waves with a velocity component opposing the flight direction will appear to be shortened. This means that a component of the wave field with true wavenumber vector **k** will appear Doppler shifted to an apparent wavenumber:

$$\mathbf{k}_{\mathrm{app}} = \mathbf{k} - |\mathbf{k}|\frac{C}{V_a}\hat{\mathbf{n}}, \tag{17}$$

where C is the phase speed of the waves, while V_a and $\hat{n}$ are the magnitude and unit direction vector of the aircraft velocity.

In water depths up to $h = 10$ m, linear waves can have phase velocities up to $C \sim (gh)^{(1/2)} \sim 10$ m s^{-1}. For a flight speed of $V_a = 56$ m s^{-1}, this implies Doppler shifts of up to $C/V_a \sim 18\%$. Clearly this is an important effect, which would need to be accounted for before accurate wavenumber information can be extracted from ALS data. For example, inspection of the swath-2.6 data in Fig. 2 shows a predominant swell with apparent wavelength of approximately 110 m, propagating at 33° from the transect direction. This corresponds to an apparent wavenumber $|\mathbf{k}_{\mathrm{app}}| = 0.057$ rad m^{-1}, with components $\mathbf{k}_{\mathrm{app}} = (0.048, 0.031)$ rad m^{-1} in the along-track and cross-track directions, respectively. Similarly, the predominant swell in the swath-2.9 data (Fig. 3) has an apparent wavelength of approximately 150 m, propagating at 42° from the

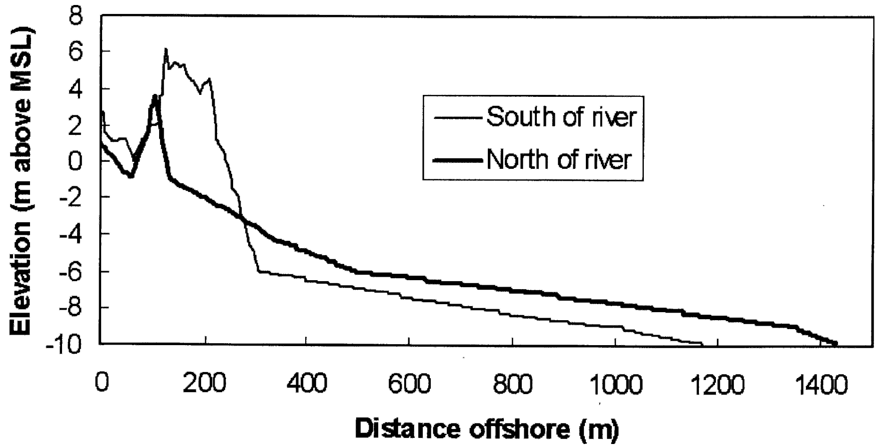

FIG. 4. Shore-normal seabed profiles surveyed in 1977 at the Waitaki river mouth (elevation relative to Lyttelton mean sea level datum).

transect direction. The corresponding apparent wavenumber is $|\mathbf{k}_{app}| = 0.042$ rad m^{-1}, with components $\mathbf{k}_{app} = (0.031, 0.028)$ rad m^{-1}. As swath 2.6 was recorded flying seaward, and swath 2.9 flying landward, it appears that much of the difference between apparent wavenumbers is due to equal and opposite Doppler shifts in the along-track wavenumber component. These values are consistent with the expected Doppler shifts for a common true wavenumber $\mathbf{k} \sim (0.04, 0.03)$ rad m^{-1}, if we use the limiting value $C = 10$ m s^{-1} appropriate for 10-m water depth. As actual wave speeds going into shallower water will be somewhat lower, it is likely that some genuine change in peak wavenumber also occurred.

We should note that Doppler shifts in the cross-track direction can also be considered, but the ground speed with which the tracking beam crosses the swath is sufficiently high (about 45 km s^{-1} in this case) to render this negligible.

While it was possible to make the estimates above, in the absence of detailed wave speed information it was not possible to accurately compute full Doppler shift corrections to the ALS data. This means that all Fourier and wavelet analysis was in effect carried out in "apparent wavenumber" space and should be interpreted accordingly.

5. Directional continuous wavelet transform of Waitaki River ALS data

ALS data from swath 2.9 were gridded by averaging data within each cell of a 166×295 cell grid at 5-m resolution, aligned with the flight direction (Fig. 3). The shoreline was subsequently masked out. The wavelet transform is most conveniently carried out on a square grid, with equal spacing and number of cells in the x and y directions. We also note that in one-dimensional wavelet transforms, errors can be caused near the ends of a data sequence by the abrupt start and end of the data (Torrence and Compo 1998). This can be partly ameliorated by zero padding up to a record length that is a power of 2, optimizing the efficiency of the fast Fourier transform.

The two-dimensional swath data came from a spatial domain with irregular edges. This means that either truncation or zero padding is unavoidable in preparing a rectangular array for analysis. For this dataset, directional wavelet spectra were computed after zero-padding the data to a 512×512 cell grid. After the wavelet transform was computed the zero-padded areas were discarded.

Morlet wavelet parameters of $\varepsilon = 1$ (isotropic), and $k_0 = 5.6$ were used, following previous studies (e.g., Spedding et al. 1993), which have found satisfactory results with $5 \leq k_0 \leq 6$. Wavelet spectra were computed at 10° increments in direction, with the scale set at $a = 2^s$, with power s ranging from 1 to 6 at uniform intervals of ¼. That is, the intervals between fully independent power-of-two scales were subdivided into four "voices." The shortest length scale examined is 2 times the spacing of the 5-m grid onto which ALS data were averaged. Because of the high wavenumber selectivity of the wavelet transform, any sea surface variation at shorter scales (<5 m) that might have been retained by sampling at higher resolution would effectively be averaged out by the transform.

Errors induced by edge effects occur over a distance from the domain boundary to a length scale proportional to the wavelet scale a (Torrence and Compo 1998). If we were to imagine including missing data from beyond the domain boundary, this would make a certain contribution to the wavelet spectral density, with the magnitude of the contribution decreasing exponentially with distance from the boundary. For the Morlet wavelet, the e-folding length, over which wavelet power drops by a factor e^{-2}, is given by $2^{1/2}a\delta x$.

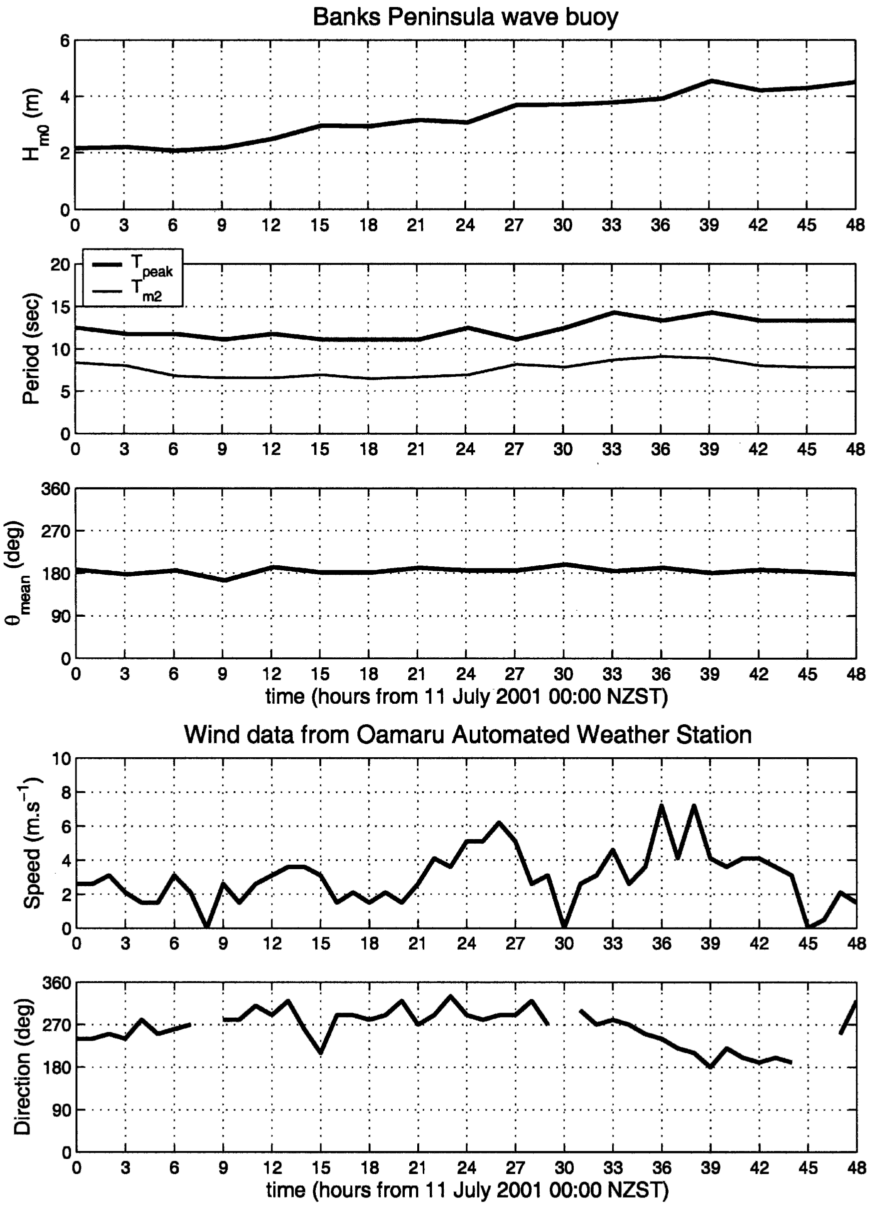

FIG. 5. (top three panels)Wave statistics [(top) significant wave height, (middle) peak and mean period, and (bottom) mean direction] recorded at the Banks Peninsula wave buoy. (bottom two panels) (top) Wind speed and (bottom) direction recorded at Oamaru, during 11–12 Jul 2001.

For $k_0 = 5.6$, the e-folding length is 1.28 times the wavelength associated with the scale.

Figure 6 shows the spatial distribution of wavelet spectral density $F(k, \theta, \mathbf{b}) = |S(a, \theta, \mathbf{b})|^2$, derived from swath-2.9 data (collected on 12 July 2001). We found that for this swath, the highest spectral densities occurred for $\theta = 40°$ and $a = 26.91$, corresponding [(12)] to a wavelength (λ) of 149 m. Contour plots are shown for a range of fixed values of a and θ around this peak. The direction θ is taken clockwise from the y axis of the local grid, and so the corresponding wave propagation direction relative to true north is $\theta_0 + (\theta \pm 180°)$, where $\theta_0 = -76.7°$ is the grid orientation. The 180° ambiguity cannot be resolved from a single image, but we would infer that $\theta = 40° \pm 10°$ corresponds to waves from 143.3° $\pm$ 10° true. Spectral densities at all other scales and directions computed, but not plotted in Fig. 6, were small (less than the second or third contour level shown here). This includes the signature of the wind sea, which we shall return to later. For now we shall concentrate on properties of the wavelet spectrum around the swell peak.

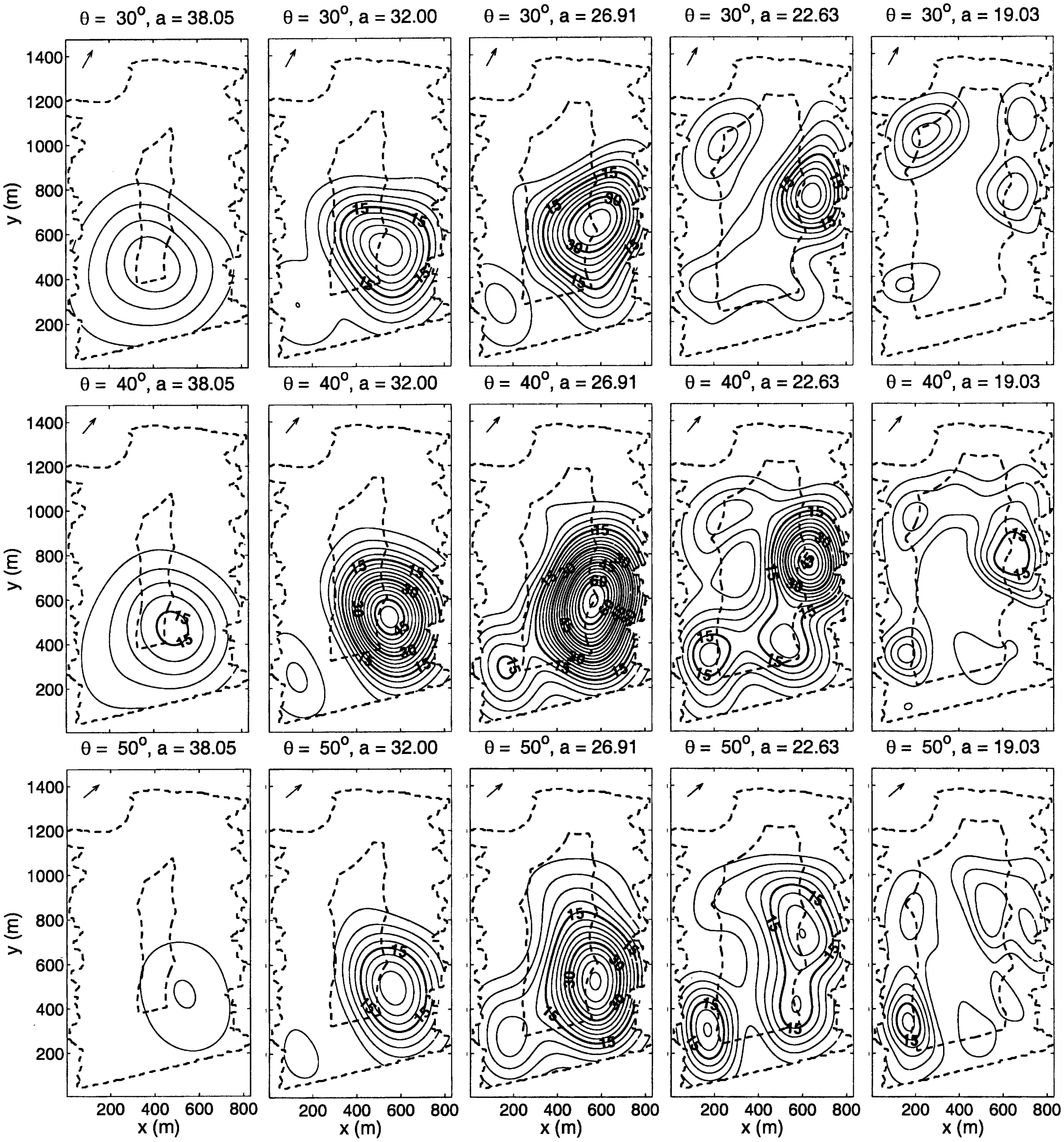

FIG. 6. Contour plots of wavelet spectral density $F(k, \theta, \mathbf{b}) = |S(a, \theta, \mathbf{b})|^2$ (m^4) computed from ALS data collected in swath 2.9. Plots are for fixed values of scale a [decreasing from (left) $a = 38.05$ to (right) $a = 19.03$] and direction θ [increasing from (top) $\theta = 30°$ to (bottom) $\theta = 50°$], with a uniform contour spacing across all plots. The direction is also indicated by arrows in the top-left corners of the plots. Dashed contours mark the boundary of the domain for which ALS data were available and the e-folding distance $(2)^{(1/2)}a\Delta x$ in from the domain boundary.

It can be seen that wavelet spectral density is strongly localized, at space scales of order one wavelength. At the peak scale-direction combination ($\theta = 40°$, $a = 26.91$), for example, the spatial distribution is dominated by one envelope of quasi-Gaussian form. For comparison, a two-dimensional Gaussian distribution

$$F(x, y) = F_0 + F_1 \exp -\frac{1}{2}\left(\frac{x_r^2}{l_1^2} + \frac{y_r^2}{l_2^2}\right) \qquad (18)$$

with rotated coordinates

$$\begin{pmatrix} x_r \\ y_r \end{pmatrix} = \begin{pmatrix} \cos\phi & \sin\phi \\ -\sin\phi & \cos\phi \end{pmatrix} \begin{pmatrix} x - x_0 \\ y - y_0 \end{pmatrix} \tag{19}$$

was fitted to the wavelet spectral density around the peak. The fitting procedure varies the parameters (x_0, y_0, l_1, l_2, ϕ, F_0, F_1) to minimize

$$\frac{\chi^2}{\sigma^2} = \frac{\sum(F_{\text{fit}} - F)^2}{\sum(F - \langle F\rangle)^2} \tag{20}$$

using the simplex method of Nelder and Mead (1965). It was found that the Gaussian function provided a close match ($\chi^2/\sigma^2 = 0.01$) with the wavelet spectral density (Fig. 7). The fitted Gaussian distribution was centered at $(x, y) = (563, 573)$, with a semimajor axis of $l_1 = 201$ m aligned at $\phi = 14°$ (26° from the propagation direction θ), and a semiminor axis of $l_2 = 138$ m. In addition to this main peak, there is a smaller quasi-Gaussian envelope evident in the bottom-left corner of the swath (Fig. 6).

A further function of sech^2 shape

$$F(x, y) = F_0 + F_1\,\text{sech}^2\left[\sqrt{\frac{1}{2}\left(\frac{x_r^2}{l_1^2} + \frac{y_r^2}{l_2^2}\right)}\right] \tag{21}$$

was also fitted to the main peak, in the light of theoretical results from solutions of the nonlinear Schrödinger equation (Hui and Hamilton 1979). This provides a somewhat narrower envelope than either the computed wavelet spectral density or the Gaussian fit (Fig. 7).

The calculation of the shape of the envelope will be affected by its proximity to the edge of the swath. As noted above, we can expect a deficit in the spectral density due to the absence of data beyond the domain boundary. The peak of the computed envelope is near the e-folding distance for such contributions to S (marked on Fig. 6), so any boundary error in $|S|^2$ will be diminished by a factor $e^{-2} = 0.135$ there. Hence, any such errors are unlikely to significantly affect the general form of the envelope near its peak, but the distribution may be distorted near the domain boundary.

The wavelet spectral density at other directions and scales also takes the form of one or more envelopes of quasi-Gaussian form. However, the location and shape of these peaks do not in general match closely across wavelet scales and directions. Gaussian functions were fitted to the most prominent peaks in the wavelet spectral densities plotted in Fig. 6. The resulting parameters are listed in Table 1. The location and dimensions of the envelope at the dominant values ($\theta = 40°$, $a = 26.91$) are approximately reproduced (with diminished magnitude) for neighboring propagation directions ($\theta = 30$–$50°$, $a = 26.91$) and at the next longer scale ($\theta = 30$–$50°$, $a = 32.0$, corresponding to a wavelength of 177 m), but with a slight seaward displacement (by 40–100 m) at the longer scale. The envelopes at the next lower scale ($a = 22.63$, corresponding to a wavelength of 125 m) show a more pronounced shoreward displacement (by 150–190 m) relative to those of $a = 26.91$ wavelets. This displacement is of magnitude comparable to the half-widths (l_1, l_2) of the envelopes, which

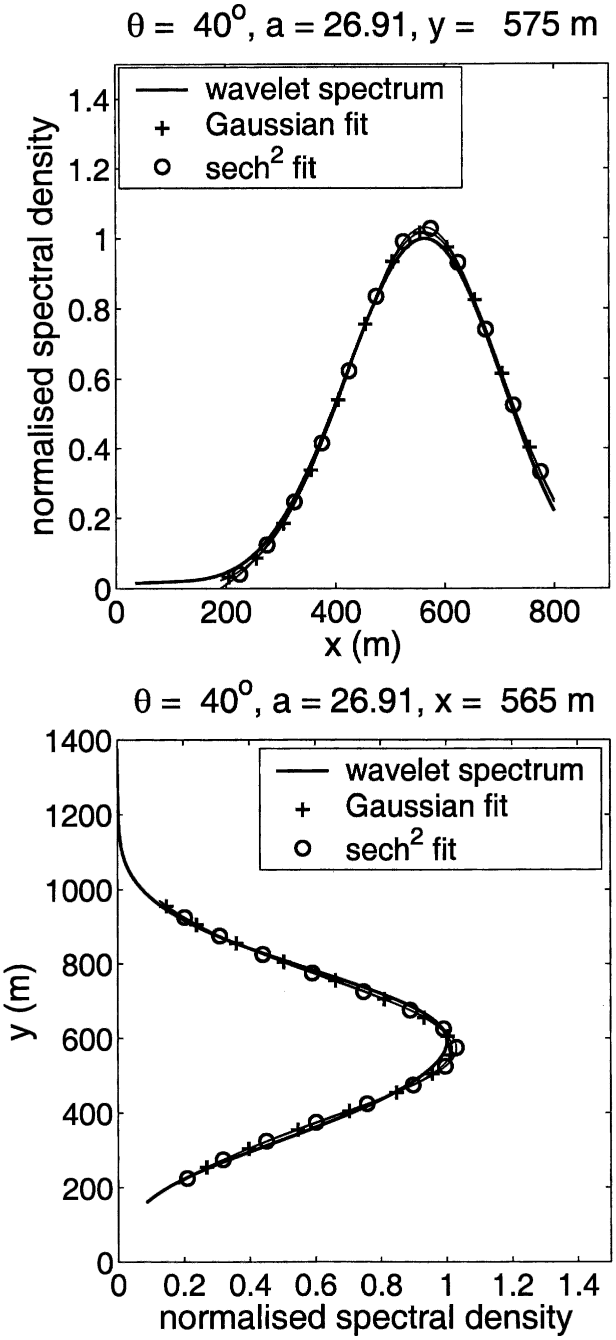

FIG. 7. Cross sections in the (top) x and (bottom) y directions through the peak of the directional wavelet spectrum $F(k, \theta, \mathbf{b}) = |S(a, \theta, \mathbf{b})|^2$, computed for direction $\theta = 40°$ and scale $a = 26.91$ from swath-2.9 data. Fitted curves using two-dimensional Gaussian and sech-squared functions are also shown.

TABLE 1. Parameters for fitting Gaussian functions [(18) and (19)] to the wavelet spectral density $F(k, \theta, \mathbf{b}) = |S(a, \theta, \mathbf{b})|^2$ computed from ALS data collected on swath 2.9 (as plotted in Fig. 6).

θ (°)	a	x_0 (m)	y_0 (m)	l_1 (m)	l_2 (m)	ϕ (°)	F_1	F_0	χ^2/σ^2
30	32.00	537	529	177	150	132	29.1	0.9	0.022
30	26.91	575	623	186	148	34	38.6	0.0	0.033
30	22.63	644	773	152	106	23	27.9	0.6	0.025
40	32.00	556	524	179	137	158	51.5	−1.3	0.007
40	26.91	563	573	201	138	14	67.8	0.0	0.010
40	22.63	627	764	149	109	5	43.0	2.1	0.010
50	32.00	571	493	184	133	159	27.2	−0.6	0.006
50	26.91	563	528	187	135	−2	40.5	2.8	0.017
50	22.63	594	746	233	127	169	22.7	1.0	0.038

are in turn of similar order to the dominant apparent wavelength. If we are to consider the sea state as consisting of an ensemble of wave groups, this places the majority of energy at this wavelet scale in the leading edge of the group envelope.

We also observe that the minor peak observed in the bottom left of the swath for the dominant ($\theta = 40°$, $a =$ 26.91) wavelet is also evident in other wavelets, most strongly around ($\theta = 50°$, $a = 22.63$), while another wave group is evident in the top left of the swath, predominantly around ($\theta = 30°$, $a = 19.03$).

Integrating the wavelet spectral densities over scale and direction results in the total energy density $E_0(\mathbf{b})$ shown in Fig. 8. A high degree of localization is still

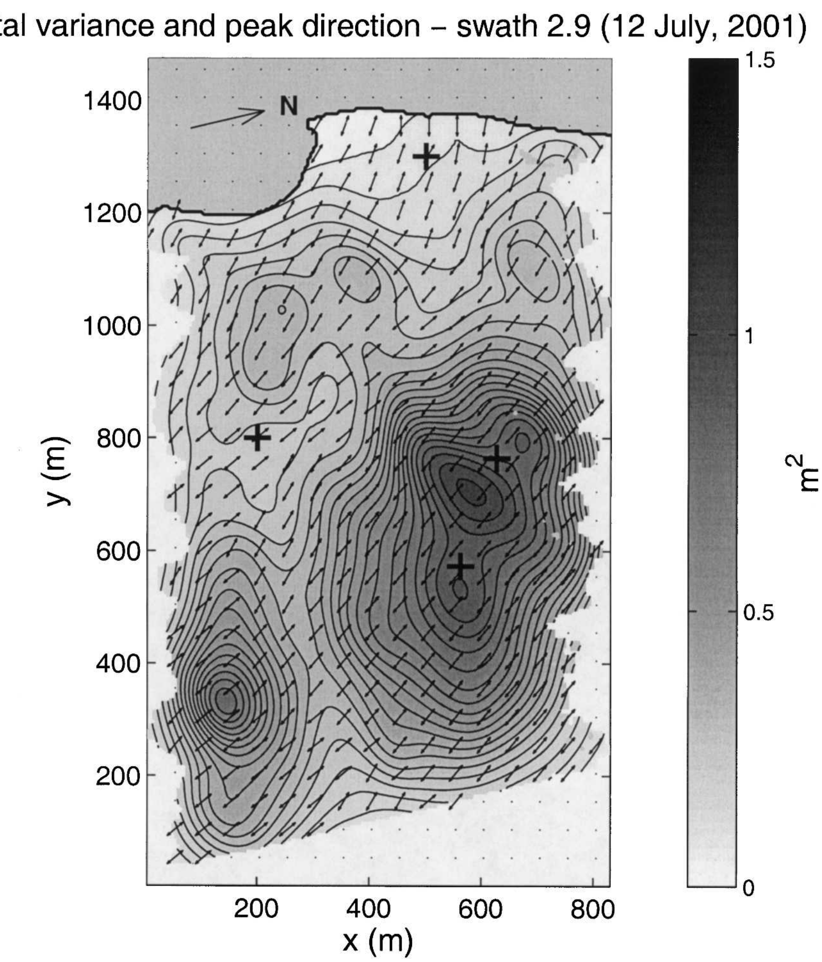

FIG. 8. Total variance $E_0(\mathbf{b})$ of the directional wavelet spectra for swath-2.9 data, with arrows showing peak direction. Four sites for which wavelet spectra are plotted in Fig. 9 are marked. The shoreline is marked by a solid line, and north is marked by an arrow.

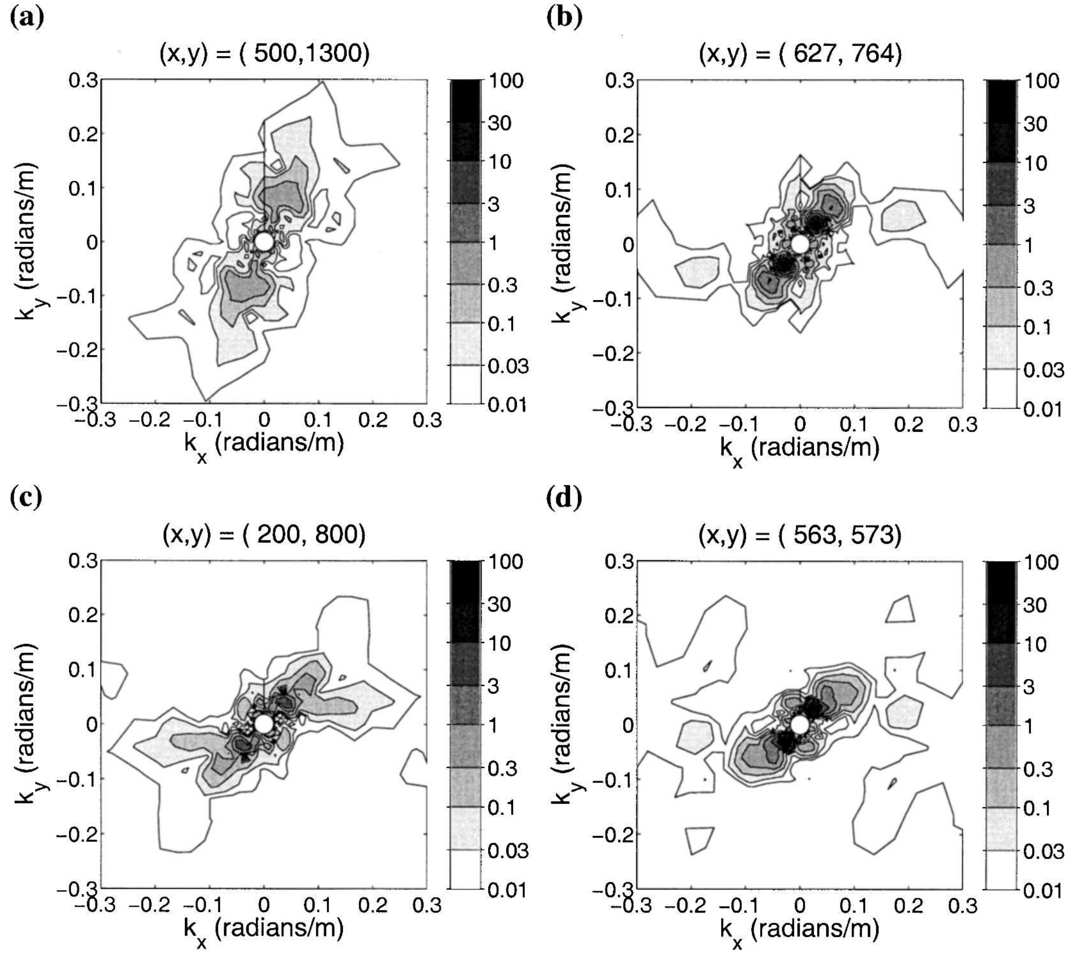

FIG. 9. Wavelet spectra $F(k, \theta, \mathbf{b})$ (m^4) at fixed locations $\mathbf{b}$ (marked on Fig. 8) from the swath-2.9 data. (a) A nearshore point $\mathbf{b}$ = (500, 1300); (b) $\mathbf{b}$ = (627, 764), the maximum of the (θ = 40°, a = 22.63) wavelet spectral density distribution; (c) $\mathbf{b}$ = (200, 800); and (d) $\mathbf{b}$ = (563, 573), the maximum of the (θ = 40°, a = 26.91) wavelet spectral density distribution.

evident, even after averaging across the offset locations of the individual wavelet scales and directions, which spreads the overall width of the envelope to cover a group of approximately 5 crests, as is evident in the original data (Fig. 3). The alignment of the peak wavenumber is also shown in Fig. 8 (up to the 180° ambiguity). This is consistent across offshore areas with higher wave energy, but shows some variation between wave groups, and also shows the effect of refraction near the coast, toward the top of the plot.

There are several ways to display the wavelet spectral density $F(k, \theta, \mathbf{b}) = |S(a, \theta, \mathbf{b})|^2$. Instead of taking slices at fixed scales and directions, the data can be localized in space, and plotted at fixed $\mathbf{b}$ as the equivalent of a directional wavenumber spectrum, up to a 180° ambiguity. In Fig. 9, this is done for four points selected from the swath 2.9 domain. Two of the points correspond to the peaks of two of the fixed (θ, a) slices discussed above. These are $\mathbf{b}$ = (563, 573) (Fig. 9d), and $\mathbf{b}$ = (627, 764) (Fig. 9b), which represent peaks in the wavelet spectral densities for (θ = 40°, a = 26.91) and for (θ = 40°, a = 22.63), respectively. Both of the directional wavelet spectra show a distinct swell peak, but this peak is offset to higher equivalent wavenumbers at the down wave point (627, 764) relative to that at (563, 573), as well as having a peak direction rotated slightly toward a more shore-normal position, and the peak spectral density reduced by a factor 2/3. There is also a small peak evident at higher wavenumber, corresponding to the southerly wind sea of approximately 30-m wavelength evident in Fig. 3.

The other points selected (Figs. 9a,c) were at a nearshore location [$\mathbf{b}$ = (500, 1300)] and a more offshore site [$\mathbf{b}$ = (200, 800)], both outside any of the group envelopes identified above. The directional wavelet spectral density is correspondingly much reduced (by 1–2 orders of magnitude) relative to the other sites. The spectrum at the nearshore site (Fig. 9a) is not only reduced in magnitude relative to those seen at the offshore sites, but rotated by refraction and broadened to contain relatively more energy at higher wavenumbers in the principal propagation direction. The wind-sea component is relatively strong at the "low energy" offshore site (Fig. 9c), but reduced near shore (Fig. 9a).

6. Conclusions

Wave fields in the sea surface show a level of inhomogeneity that is not consistent with the fully regular assembly of sinusoidal waves of various amplitudes, wavelengths and directions implied by the Fourier approach. It is therefore valuable to seek a description of the sea state that identifies and quantifies the spatially periodic signals present, but also localizes that signal in space. A method based on two-dimensional directional wavelet analysis is described by which such inhomogeneity can be characterized in the spatial and wavenumber domains. When this method has been applied to aerial laser scanning measurements of near shore wave conditions, it has allowed a high level of spatial variability to be observed. Evidence was found of ensembles of wave group envelopes of quasi-Gaussian form. It was also noted that the spatial localization of these envelopes is not necessarily uniform across the various spatial scales and propagation directions of wave components making up the groups. Rather, examples were found of components with length scales shorter than those of the peak being displaced in the down wave direction relative to the envelope of energy distribution at the dominant length scale.

ALS records of the sea surface can be influenced by Doppler effects due to the relative motions of waves and the scanning aircraft. Estimation of the magnitude of such effects can be made, and we have found for example that much of the apparent difference in wavenumber structure between swaths 2.6 and 2.9 (recorded with opposite flight directions) can be attributed to Doppler effects. While distortions can arise, features such as the shoreward displacement of wave envelopes noted above cannot simply be Doppler artifacts, as evidenced by their occurrence in swaths recorded in both flight directions. Given adequate wave speed information, correction for Doppler effects should be considered in future studies.

The directional wavelet transform provides a valuable analytical tool for studies of the spatial structure of sea states. Allowing a selective balance between spatial resolution and spectral resolution, it has a potential role in filtering spatial data for studies of wave processes. It could also assist in developing models that accurately reflect the group structure of surface wave fields.

Acknowledgments. This work was carried out with the support of the New Zealand Foundation for Research, Science and Technology (Contract Number C01X0218). Aerial Laser Scanning was carried out by AAM Geoscan (Brisbane, Australia). We thank Meridian Energy, Ltd., for use of the data. We thank Rob Bell and Murray Smith for their comments on the manuscript.

APPENDIX

Calculation of c_ψ

The normalization parameter c_ψ is defined as

$$c_\psi = (2\pi)^2 \int \frac{d^2\mathbf{k}}{|\mathbf{k}|^2} |\hat{\psi}(\mathbf{k})|^2. \tag{A1}$$

For the Morlet wavelet, we have (Antoine and Murenzi 1996; Antoine et al. 1996)

$$|\hat{\psi}_M(\mathbf{k})|^2 = \varepsilon \exp\{-[\varepsilon k_x^2 + (k_y - k_0)^2]\} \times [1 - \exp(-k_y k_0)]^2, \tag{A2}$$

and so the normalization parameter can be expressed as

$$c_\psi = (2\pi)^2 \varepsilon \int_{-\infty}^{+\infty} ds \int_{-\infty}^{+\infty} dt \exp[-(\varepsilon s^2 + t^2)] F(s, t) \tag{A3}$$

with

$$F(s, t) = \frac{\{1 - \exp[-k_0(k_0 + t)]\}^2}{s^2 + (k_0 + t)^2}, \tag{A4}$$

where we have made the substitutions $s = k_x$ and $t = k_y - k_0$.

While the denominator of F vanishes at $(s, t) = (0, -k_0)$ $[(k_x, k_y) = (0, 0)]$, the numerator does also; in such a way that F remains finite. The variation of the integrand is dominated by the exponential function, and decays rapidly away from the maximum at $(s, t) = (0, 0)$. Hence, if we take a Taylor expansion of F about $(0, 0)$:

$$F(s, t) = F(0, 0) + sF_s(0, 0) + tF_t(0, 0) + \frac{s^2}{2!} F_{ss}(0, 0) + \frac{2st}{2!} F_{st}(0, 0) + \frac{t^2}{2!} F_{tt}(0, 0) + \cdots, \tag{A5}$$

we expect only the low-order terms to contribute significantly to the integrand. The integral can then be expressed as

$$c_\psi = c_\psi^{(n)} + R^{(n)}, \tag{A6}$$

where

$$c_\psi^{(n)} = (2\pi)^2 \varepsilon \int_{-\infty}^{+\infty} ds \int_{-\infty}^{+\infty} dt \exp[-(\varepsilon s^2 + t^2)] F^{(n)}(s, t) \tag{A7}$$

TABLE A1. Values of c_ψ computed for the Morlet wavelet with various values of the parameters ε and k_0. The contributions of the Taylor series terms $c_\psi^{(n)}$ are shown to zeroth, second, and fourth order, along with the fourth-order remainder term $R^{(4)}$.

ε	k_0	c_ψ	$c_\psi^{(0)}$	$c_\psi^{(2)}$	$c_\psi^{(4)}$	$R^{(4)}$
0.5	5.0	3.5328	3.5080	3.5781	3.5318	0.0010
0.5	5.6	2.8180	2.7965	2.8411	2.8177	0.0004
0.5	6.0	2.4546	2.4361	2.4699	2.4544	0.0002
0.5	7.0	1.8019	1.7898	1.8080	1.8019	0.0001
1.0	5.0	5.1379	4.9610	5.1594	5.1356	0.0023
1.0	5.6	4.0698	3.9549	4.0810	4.0689	0.0009
1.0	6.0	3.5334	3.4451	3.5408	3.5329	0.0005
1.0	7.0	2.5798	2.5311	2.5828	2.5796	0.0001
2.0	5.0	7.3733	7.0159	7.3667	7.3688	0.0045
2.0	5.6	5.8188	5.5930	5.8160	5.8171	0.0017
2.0	6.0	5.0430	4.8722	5.0413	5.0420	0.0010
2.0	7.0	3.6714	3.5796	3.6709	3.6711	0.0003

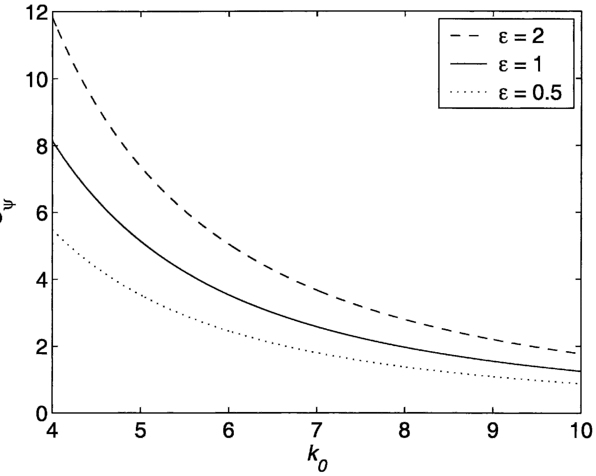

FIG. A1. Normalization parameter c_ψ as a function of k_0 and ε, computed using a fourth-order Taylor series expansion [(A12)].

is the integral with the Taylor series for F retaining terms to order n, while

$$R^{(n)} = (2\pi)^2\varepsilon\int_{-\infty}^{+\infty} ds \int_{-\infty}^{+\infty} dt \exp[-(\varepsilon s^2 + t^2)] \times [F(s,t) - F^{(n)}(s,t)] \tag{A8}$$

is a remainder term. This can be computed by numerical quadrature with small errors, due to a high level of cancellation in the integrand. Further, due to the symmetry of the integration domain, Taylor series terms odd in s and/or t will integrate to zero. The $c_\psi^{(n)}$ terms can be computed analytically, making use of the identity

$$I_n(a) = \int_{-\infty}^{\infty} dx\, x^{2n} \exp(-ax^2) = \frac{1 \times 3 \times 5 \times \cdots \times (2n-1)}{2^n a^n}\sqrt{\frac{\pi}{a}} \tag{A9}$$

(Abramowitz and Stegun 1970).

Retaining just the zeroth-order term,

$$c_\psi^{(0)} = (2\pi)^2\varepsilon\int_{-\infty}^{+\infty} ds \int_{-\infty}^{+\infty} dt \exp[-(\varepsilon s^2 + t^2)]F(0,0) = 4\pi^3\sqrt{\varepsilon}\left[\frac{1}{k_0^2}(1 - e^{-k_0^2})^2\right]. \tag{A10}$$

Retaining up to the second-order term,

$$c_\psi^{(2)} = (2\pi)^2\varepsilon\int_{-\infty}^{+\infty} ds \int_{-\infty}^{+\infty} dt \exp[-(\varepsilon s^2 + t^2)]\left[F(0,0) + \frac{1}{2}s^2F_{ss}(0,0) + \frac{1}{2}t^2F_{tt}(0,0)\right]$$
$$= 4\pi^3\sqrt{\varepsilon}\left\{\frac{1}{k_0^2} + \frac{1}{k_0^4}\left(\frac{3}{2} - \frac{1}{2\varepsilon}\right) + e^{-k_0^2}\left[-2 - \frac{4}{k_0^2} + \frac{1}{k_0^4}\left(-3 + \frac{1}{\varepsilon}\right)\right] + e^{-2k_0^2}\left[4 + \frac{3}{k_0^2} + \frac{1}{k_0^4}\left(\frac{3}{2} - \frac{1}{2\varepsilon}\right)\right]\right\}, \tag{A11}$$

and to fourth order,

$$c_\psi^{(4)} = 4\pi^3\sqrt{\varepsilon}\left[F(0,0) + \frac{1}{4\varepsilon}F_{ss}(0,0) + \frac{1}{4}F_{tt}(0,0) + \frac{3}{4.4!\varepsilon^2}F_{ssss}(0,0) + \frac{3.6}{4.4!\varepsilon}F_{sstt}(0,0) + \frac{3}{4.4!}F_{tttt}(0,0)\right]$$
$$= 4\pi^3\sqrt{\varepsilon}\left\{\frac{1}{k_0^2} + \frac{1}{k_0^4}\left(\frac{3}{2} - \frac{1}{2\varepsilon}\right) + \frac{1}{k_0^6}\left(\frac{15}{4} - \frac{15}{2\varepsilon} + \frac{1}{4\varepsilon^2}\right) + e^{-k_0^2}\left[-16k_0^2 - \frac{5}{2} + \frac{1}{k_0^2}\left(-\frac{25}{4} + \frac{3}{4\varepsilon}\right) + \frac{1}{k_0^4}\left(3 + \frac{7}{\varepsilon}\right)\right.\right.$$
$$\left.\left. + \frac{1}{k_0^6}\left(\frac{11}{2} - \frac{15}{\varepsilon} - \frac{1}{2\varepsilon^2}\right)\right] + e^{-2k_0^2}\left[\frac{1}{2}k_0^2 + 6 + \frac{1}{k_0^2}\left(\frac{15}{2} - \frac{3}{2\varepsilon}\right) + \frac{1}{k_0^4}\left(-\frac{9}{2} - \frac{13}{2\varepsilon}\right) + \frac{1}{k_0^6}\left(\frac{15}{4} - \frac{15}{2\varepsilon} + \frac{1}{4\varepsilon^2}\right)\right]\right\}. \tag{A12}$$

For typical values of $k_0 > 5$, the exponential terms are negligible, and so the contribution from nth-order terms is of order ${k_0}^{-2-n}$. Some numerical examples of c_ψ computed in this way are listed in Table A1. At $k_0 = 5.6$ and $\varepsilon = 1$, for example, we see that values computed with Taylor series to zeroth order (A10), second order (A11), and fourth order (A12) have errors of 2.82%, 0.28%, and 0.02%, respectively. The fourth-order estimate $c_\psi^{(4)}$ is plotted as a function of k_0 and ε in Fig. A1.

REFERENCES

Abramowitz, M., and I. A. Stegun, 1970: *Handbook of Mathematical Functions*. 9th ed. Dover, 1046 pp.

Antoine, J.-P., and R. Murenzi, 1996: Two-dimensional directional wavelets and the scale-angle representation. *Signal Proc.,* **52,** 259–281.

——, ——, and P. Vandergheynst, 1996: Two-dimensional directional wavelets in image processing. *Int. J. Imaging Syst. Technol.,* **7,** 152–165.

Argoul, F., A. Arneodo, J. Elezgaray, G. Grasseau, and R. Murenzi, 1989: Wavelet transform of fractal aggregates. *Phys. Lett. A,* **135,** 327–336.

Chui, C. K., L. Montefusco, and L. Puccio, 1994: Wavelets: Theory, algorithms, and applications. Vol. 5, *Wavelet Analysis and Its Applications*, Academic Press, 627 pp.

Daubechies, I., 1990: The wavelet transform, time-frequency localization and signal analysis. *IEEE Trans. Inf. Theory,* **36,** 961–1005.

——, 1992: *Ten Lectures on Wavelets*. SIAM, 357 pp.

Donelan, M. A., W. M. Drennan, and A. K. Magnusson, 1996: Nonstationary analysis of the directional properties of propagating waves. *J. Phys. Oceanogr.,* **26,** 1901–1914.

Farge, M., 1990: Transformée en ondelettes continue et application à la turbulence. Publication de la Societé de Mathématique de France, 17–62.

——, E. Goirand, and T. Philipovitch, 1993: Wavelets and wavelet packets to analyse, filter and compress two-dimensional turbulent flows. *Probability Concepts in Physical Oceanography*, P. Müller, Ed., Hawaii University Press, 131–159.

Gabor, D., 1946: Theory of communication. *J. Inst. Elect. Eng.,* **93,** 429–457.

Goupillaud, P., A. Grossmann, and J. Morlet, 1984: Cycle-octave and related transforms in seismic signal analysis. *Geoexploration,* **23,** 85–102.

Grossmann, A., and J. Morlet, 1984: Decomposition of Hardy functions into square integrable wavelets of constant shape. *SIAM J. Math. Anal.,* **15,** 723–736.

Hicks, D. M., J. Rice, S. Williams, and D. Turton, 2001: ALS stops the flow of water. *Scanning the Horizons,* No. 11, AAM Geoscan, Queensland, Australia, 1–3.

——, M. J. Duncan, U. Shankar, M. Wild, and J. R. Walsh, 2003: Project Aqua: Lower Waitaki River geomorphology and sediment transport. NIWA Client Rep. CHC01 (115), 171 pp.

Hui, W. H., and J. Hamilton, 1979: Exact solutions of a three-dimensional nonlinear Schrödinger equation applied to gravity waves. *J. Fluid Mech.,* **93,** 117–133.

Liu, P. C., 2000a: Is the wind wave frequency spectrum outdated? *Ocean Eng.,* **27,** 577–588.

——, 2000b: Wavelet transform and new perspective on coastal and ocean engineering data analysis. *Advances in Coastal and Ocean Engineering*, P. L.-F. Liu, Ed., Vol. 6, World Scientific Publishing, 57–101.

Mollo-Christensen, E., and A. Ramamonjiarisoa, 1978: Modeling the presence of wave groups in a random wave field. *J. Geophys. Res.,* **83,** 4117–4122.

Murenzi, R., 1989: Wavelet transforms associated to the n-dimensional Euclidean group with dilations: Signals in more than one dimension. *Wavelets, Time-Frequency Methods and Phase Space*, J.-M. Combes, A. Grossmann, and P. Tchamitchian, Eds., Springer-Verlag, 239–246.

Nelder, J. A., and R. Mead, 1965: A simplex method for function minimization. *Comput. J.,* **7,** 308–313.

Spedding, G. R., F. K. Browand, N. E. Huang, and S. R. Long, 1993: A 2-D complex wavelet analysis of an unsteady wind-generated surface wave field. *Dyn. Atmos. Oceans,* **20,** 55–77.

Torrence, C., and G. P. Compo, 1998: A practical guide to wavelet analysis. *Bull. Amer. Meteor. Soc.,* **79,** 61–78.

Williams, S., and D. Jonas, 2001: Heights accurate enough for drainage analysis: Ellipsoidal to orthometric heights. *Scanning the Horizons,* No. 11, AAM Geoscan, Queensland, Australia, 3–4.